PHYSICAL REVIEW B **105**, 165201 (2022)

Editors' Suggestion

Negatively charged boron vacancy center in diamond

T. Umeda,[1,*] K. Watanabe,[2] H. Hara,[3] H. Sumiya,[4] S. Onoda,[5] A. Uedono,[1] I. Chuprina,[6] P. Siyushev,[6] F. Jelezko,[6] J. Wrachtrup,[7] and J. Isoya[1]

[1] *Faculty of Pure and Applied Sciences, University of Tsukuba, Tsukuba, Ibaraki 305-8573, Japan*
[2] *National Institute for Material Science, 1-1 Namiki, Tsukuba, Ibaraki 305-0044, Japan*
[3] *Bruker Japan K. K., 3-9 Moriya, Yokohama, Kanagawa 221-0022, Japan*
[4] *Sumitomo Electric Industries, Ltd., Itami, Hyogo 664-0016, Japan*
[5] *Takasaki Advanced Radiation Research Institute, National Institutes for Quantum Science and Technology, 1233 Watanuki, Takasaki, Gunma 370-1292, Japan*
[6] *Institute for Quantum Optics and IQST, Ulm University, Albert-Einstein-Allee 11, D-89081 Ulm, Germany*
[7] *3rd Institute of Physics, Research Center SCoPE and IQST, University of Stuttgart, D-70569 Stuttgart, Germany*

(Received 26 October 2021; accepted 25 February 2022; published 4 April 2022)

Impurity-vacancy complexes in diamond are an attractive family of spin defects since NV^-, SiV^-, GeV^-, and SnV^- have emerged as promising platforms for quantum applications. Although boron is most easily incorporated into diamond, a boron-vacancy complex in the negative charge state (BV^-) has eluded experimental observation. This center was theoretically predicted as another promising spin qubit. In this work, we experimentally observed an electron paramagnetic resonance (EPR) spectrum identified as BV^- in synthetic diamonds via a Fermi-level tuning. Fingerprints of BV^- such as the spin multiplicity of $S = 1$, C_{3v} symmetry, and the zero-field splitting ($D = 2913$ MHz), in addition to ^{10}B and ^{11}B hyperfine (HF) interactions, have been confirmed. Moreover, optically pumped spin polarization has been observed with 3.0–3.6 eV excitation. However, unlike the NV^- center, the photoluminescence as well as optically detected magnetic resonance from BV^- have not been confirmed even at low temperatures. We speculate that the Jahn-Teller instability in the triplet excited states of the NV^- and BV^- centers results in different optical properties.

DOI: 10.1103/PhysRevB.105.165201

I. INTRODUCTION

With its excellent properties as a solid-state spin qubit [1], the nitrogen-vacancy center (NV^-) in diamond opens up new avenues of applications to quantum information processing [2–7], quantum communication [8–12], and quantum sensing of magnetic fields [13–15], electric fields [16,17], and temperature [18], including ultrahigh-sensitivity nuclear-magnetic-resonance (NMR) spectroscopy [19,20].

In addition to the NV^- center, various other defects have been explored in diamond, such as silicon-vacancy (SiV^-) [21–25], germanium-vacancy (GeV^-) [26,27], and tin-vacancy (SnV^-) centers [28–30]. These group-IV impurity-vacancy centers having D_{3d} symmetry with a split-vacancy configuration and a spin-1/2 ground state exhibited optical properties superior to the NV^- center, enabling us to expand the limit of diamond-based spin qubits [12,31].

On the other hand, a new family of NV^--like defects possessing C_{3v} symmetry with a pair of substitutional impurity and adjacent vacancy and triplet ($S = 1$) ground states has been searched for by replacing the nitrogen atom with a first-row element such as oxygen [32–36] and boron [32,37,38]. Figure 1(a) to 1(c) show schematic views of the one-electron state levels for the family of NV^-, OV^0, and BV^-, respectively (see Appendix A for details). Although the number of valence electrons and the number of states in the gap are different, these three centers have a common triplet ground state ($^3A_2$ many-electron state) originating from two unpaired electrons in doubly degenerate e states (denoted by "e_x" and "e_y") [1] which are localized on the dangling bonds of carbon atoms surrounding the vacancy. In fact, an electron paramagnetic resonance (EPR) center with $S = 1$ and C_{3v} symmetry, labeled "WAR5," arises from OV^0 [33,34], exhibiting a zero-field splitting (D) and ^{13}C hyperfine (HF) couplings quite similar to those of the NV^- center. First-principles calculations [35] also supported the consistency of the zero-field splittings between OV^0 (2888 MHz) [33] and NV^- (2872 MHz) [39]. On the other hand, the triplet excited state (^3E many-electron state) originates from different configurations, i.e., $(a_1)^1e^3$ for NV^-, $e^1(3a_1)^1$ for OV^0, and $e^1(a_1)^1$ for BV^-. As a result, the OV^0 and NV^- centers have quite different optical responses [33–35]. For NV^-, an optical excitation above 1.945 eV (conventionally 532-nm or 2.33-eV excitation is used) easily enhances its EPR signal due to spin polarization. This optical-pumping ability enables the spin qubit initialization of the NV^- center. Unfortunately, no spin polarization was observed for OV^0 [33,34]. First-principles calculations predicted a fast nonradiative decay caused by a distortion of the excited state to a configuration of two covalent C-O bonds and one elongated C-O bond, making OV^0 nonluminescent or weakly luminescent [35]. Accordingly, the OV^0 center has

---

[*] Corresponding author: umeda.takahide.fm@u.tsukuba.ac.jp

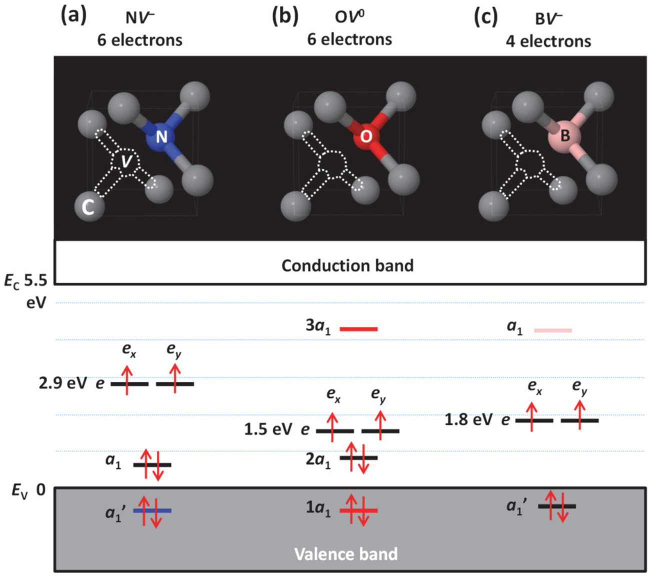

FIG. 1. Electronic configurations of three analog color centers in diamond. (a) NV^- center with six valence electrons. (b) OV^0 center with six valence electrons. (c) BV^- center with four valence electrons. Within a defect-molecular-orbital model (see Appendix A), one-electron states a_1 (black color) and a_1' (color of each impurity) dominantly originate from atomic orbitals of carbon and impurity atoms, respectively [1]. Doubly degenerate e states also comprise two carbon-related orbitals (denoted by e_x and e_y) adjacent to a vacancy [1]. In the OV^0 center, a_1' and a_1 are rewritten by $1a_1$ and $2a_1$, respectively, and another a_1' state (denoted by $3a_1$) is generated from an antibonding state of C-O bonds with three back-bonded carbon atoms [35]. Their energy positions are approximately shown in a band diagram [1,32,35–37], where E_C and E_V are the conduction-band top and the valence-band bottom, respectively.

presumably been excluded from the candidates of NV-akin solid-state spin qubits [35].

As shown in Fig. 1(c), the BV^- center with four valence electrons also realizes a spin-1 system with the e_x and e_y levels [32,37,38], which is exactly identical to those of NV^- and OV^0. First-principles calculations predicted that the BV^- center is optically active with a triplet ground state and a triplet excited state in the band gap, suggesting it is a promising spin qubit [37,38]. Since both boron and nitrogen atoms are the most major impurities in diamond, the BV^- center might have potential comparable to that of the promising NV^- center. Despite B-doped diamonds being as widely used as N-doped diamonds, there are no reports of the BV^- center being found in diamond.

Here, we experimentally demonstrate that the BV^- center is successfully formed in electron-irradiated and annealed high-pressure–high-temperature (HPHT) grown diamond crystals with N and B codoping, and that it even exhibits a desired spin-1 system ($D = 2913$ MHz and C_{3v} symmetry) resembling that of NV^-. Moreover, the BV^- center shows an optically induced spin polarization with 3.0-eV optical pumping. Using a combination of EPR imaging, photoluminescence (PL), and cathodoluminescence (CL) microscopy, we suggest a preferential formation of the BV^- center in a specific area of diamond, distributing separately from the NV^- center. Such different formation behaviors will provide a hint as to the selective formation of the BV^- and NV^- centers.

Using above-3.0-eV optical pumping, optical absorption with a spin-conserving transition can be activated for BV^-. Subsequently, we have performed confocal microscope (CFM) experiments to identify PL lines of BV^-, which is essential for optically addressing individual spin qubits. This trial, however, was not successful due to too weak luminescence from the BV^- centers. Our experimental results suggest that, even though the BV^- and NV^- centers have the analog ground states, radiative and nonradiative decays from their triplet excited states are quite different.

II. EXPERIMENT

We prepared two N and B codoped HPHT diamonds. Two (100)-oriented plates weighing 76.7 mg (plate-I) and 78.9 mg (plate-II) were prepared by laser-cutting of two HPHT type-IIa diamond crystals. Both crystals were grown by the temperature gradient method at high pressure (5.5 GPa) and high temperature (1350 °C) using a metal solvent of Fe-Co alloy with Ti added as a nitrogen getter. The boron impurities were incorporated into the crystals via the solid carbon source [40]. The two crystals were irradiated with 3 MeV electrons at room temperature to total fluences of 2×10^{17} and 4×10^{17} e/cm^2, respectively, and they were annealed at 850 °C for 2 h in vacuum, converting small fractions of the impurities into the NV^- and BV^- centers.

The two diamond samples were characterized by EPR spectroscopy. Continuous-wave (cw) EPR spectra were measured by a Bruker E500 X-band spectrometer with a Bruker ER4122SHQ cavity (the loaded Q-factor was $Q_L \sim 10\,000$) and with an Oxford Instruments ESR900 He cryostat. In the case of paramagnetic centers studied in this paper [i.e., the $P1$ center or $\mathrm{N_s}^0$ ($S = 1/2$), the NV^- center ($S = 1$), and the BV^- center ($S = 1$) with low concentrations], the standard slow-passage measurements (saturation-free measurements) were not suitable because of a severe drawback in the signal sensitivity. Therefore, we used rapid-passage (RP) measurements [41], which allow a stronger microwave excitation, achieving a much higher signal sensitivity. This technique utilized the passage effect, which is induced by a rapid scan of the magnetic field faster than the electron spin relaxation rates [41].

The RP technique has been developed by the group at the University of Warwick for quantifying low concentrations of $\mathrm{N_s}^0$ in diamond. It combines a rapid scan of the external field (~10 mT/s) with an out-of-phase detection with respect to 100-kHz field modulation [33,42]. By using this technique, absorption-form EPR spectra are obtained as shown in Fig. 2(a). The RP measurements often give us a much higher sensitivity: for instance, the detection limit for $\mathrm{N_s}^0$ was extended to 0.02 ppb for a sample of $\sim 10\,\mathrm{mm}^3$ volume after appropriate signal averaging [42]. Thus, we used this technique for quantifying spin concentrations or observing weak ^{10}B HF structures.

Moreover, we used another technique, denoted the "out-of-phase method," which records an out-of-phase first-harmonic signal with respect to 100-kHz field modulation under a slow scan of the external field [43,44]. This technique generates

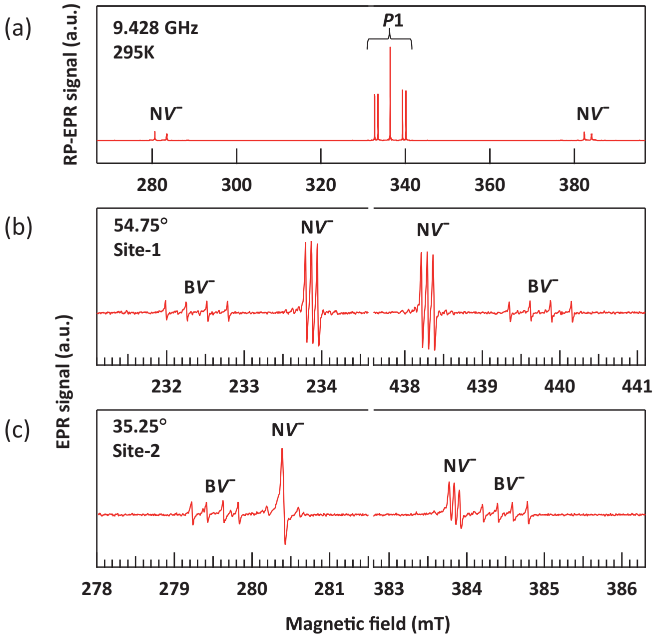

FIG. 2. EPR spectra of N and B codoped diamond. (a) Rapid-passage (RP) EPR spectrum shows EPR signals of NV^- ($S = 1$), in addition to strong primary signals of $P1$ (N$_{\rm s}{}^0$, $S = 1/2$). This spectrum was recorded for a magnetic-field angle $\theta = 90°$. (b), (c) Magnified EPR spectra show low- and high-field side EPR signals of NV^- as well as those of BV^- with a fourfold splitting. These spectra were recorded at two principal-axis directions. At 54.75° with $\boldsymbol{B}$ // [111], a site-1 center [cf., Fig. 3(a)] of BV^- or NV^- shows its symmetry axis parallel to $\boldsymbol{B}$. On the other hand, at 35.25°, $\boldsymbol{B}$ is perpendicular to a symmetry axis of site-2-type BV^- and NV^- centers [cf., Fig. 3(a)]. Out-of-phase EPR spectra (slow passage) were recorded by using a field-modulation amplitude of 0.004 mT, microwave power of 0.1 mW, and an accumulation of 8–13 h.

first-derivative EPR spectra as shown in Figs. 2(b) and 2(c). Because of the slow field scan, the out-of-phase method enables us to measure resonant positions accurately, which is beneficial in determining the spin-Hamiltonian (SH) parameters.

By using the RP method, the average concentrations of the $P1$, NV^-, and BV^- centers in each crystal (labeled [N$_{\rm s}{}^0$]$_{\rm avg}$, [NV^-]$_{\rm avg}$, and [BV^-]$_{\rm avg}$, respectively) are estimated to be 90, 9, and 1.5 ppb for plate-I, and 110, 15, and 2 ppb for plate-II, respectively. The subscript "avg" indicates that these HPHT plates have nonuniform distributions of impurities, which are proven by EPR imaging.

In addition to conventional EPR measurements, photo-EPR and EPR imaging have been performed. Photo-EPR measurements were performed by irradiating a monochromatic light (0.50–5.50 eV or 2480–225 nm) extracted from a 150-W xenon lamp source. An energy step was set to 0.1 eV, which is larger than the resolution of our monochromator. In photo-EPR measurements, EPR spectra under illumination are recorded as a function of the photon energy. A change of EPR signal is caused by either optical spin polarization [45,46] or the change of the charge state [47,48]. In the former change, the threshold of the optical pumping matches the zero-phonon line (ZPL) of the optical absorption band [45,46]. When the latter change is caused by a transition between the defect level and the valence band (or the conduction band), the photoexcitation threshold indicates the position of the defect level or the ionization energy of the defect [47,48].

EPR imaging was performed by using a high-power gradient accessory Bruker E540 GCX2 [two-dimensional (2D) gradients with 20 mT/cm] and a Bruker ER4108 TMHS resonator. In the present 2D EPR imaging, field-swept cw-EPR spectra are taken under the main external magnetic field ($B_{\rm ext}$) along the z axis with superimposing the magnetic field gradient (MFG) parallel to the yz plane. The MFG is generated by two gradient coils along the y and z axes. Then, the same paramagnetic species at different yz positions are resonant at different $B_{\rm ext}$ values. A 2D EPR image is reconstructed from a set of projections acquired at different directions of constant MFG. The narrower linewidth and stronger MFG provide a higher spatial resolution. EPR imaging visualizes a spatial distribution of paramagnetic species in a sample [49,50]. Thus, EPR imaging is useful in revealing the growth sector dependence of impurity incorporation and the formation of radiation defects in diamond [51,52]. We studied the spatial distribution of N$_{\rm s}{}^0$ ($S = 1/2$) and NV^- ($S = 1$) in plate-II. For recording 2D EPR imaging, the main uniform field, $\boldsymbol{B}_{\rm ext}$, was set to be the [011] direction, where the $P1$ spectrum consists of five split lines and the NV^- spectrum (low-field side) reveals two split lines, as shown in Fig. 2(a). Since their EPR signals are very well separated, individual distributions are easily obtained. Full five-line spectra were used for reconstructing the 2D distribution of N$_{\rm s}{}^0$, and the low-field-side spectra were collected for the NV^- center. The NV^- signals were enhanced ~100 times under illumination of a 532-nm laser light. RP cw-EPR spectra were obtained by sweeping the main uniform field ($\boldsymbol{B}_{\rm ext}//z$) and were collected by varying a constant MFG in the yz plane stepped for 196 directions spanning 180°. The MFG started from the z axis (the [011] direction) to the $-z$ axis via the y axis (the [0$\bar{1}$1] direction). The field gradients used were 2.5 mT/cm for N$_{\rm s}{}^0$ and 2.0 mT/cm for NV^-. A set of projection spectra were collected in ~75 min.

We also carried out PL and CL measurements to further reveal inhomogeneous distributions of the impurities and defects. The PL spectra were measured at room temperature with excitation by the 514.5 nm line of an Ar-ion laser. The signals were dispersed with a monochromator (Jobin Yvon, HR-320) and detected by a liquid-nitrogen-cooled charge-coupled device (CCD) (Roper, LN/CCD-400EB-GI). The spectral resolution of the monochromator is less than 0.5 nm. The CL spectra were measured at 83 K by using a system consisting of a scanning electron microscope (Topcon, SM-350) equipped with an optical window, optics coupled to a spectrograph (Photon Design Co., PDP-320), and a liquid-nitrogen-cooled CCD (Roper, LN/CCD-400EB-GI). The spectral resolution of the spectrograph is less than 0.5 nm.

Additionally, attempts to identify PL of the BV^- centers were carried out using CFM. We utilized a home-built CFM combined with a continuous-flow He cryostat (CryoVac) operating at 4 K. To match the absorption band found in EPR spin-polarization experiments, laser excitation at 375 nm (3.31 eV) was used. The PL collected from the sample was sent either to the photomultiplier tube (Hamamatsu

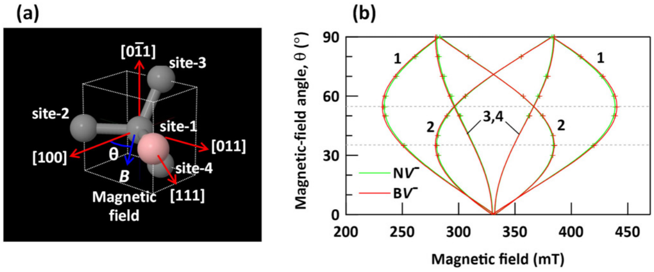

FIG. 3. (a) Experimental coordinate and corresponding atomic configurations of the BV^- and NV^- centers. A single impurity atom is located at one of the site-1 to site-4 positions, and a monovacancy is inserted into the origin of the coordinate. In EPR experiments, the external magnetic field (***B***) was rotated in the (0$\bar{1}$1) plane from $\theta = 0^\circ$ at ***B*** // [100] to $\theta = 90^\circ$ at ***B*** // [011]. (b) Angular dependences of EPR signal positions of BV^- and NV^-. "+" symbols and solid lines express experimental data and theoretical curves, respectively. Both of the spin-1 systems of BV^- and NV^- show the same C_{3v} symmetry and very similar **D** tensors. Numbers in the figure denote the site number. The site-3 and -4 centers are always indistinguishable within the ***B*** rotation in the (0$\bar{1}$1) plane.

H10682-210) for imaging or to the spectrometer (Princeton Instruments) for the light PL analyses. To reject the reflected laser light in the detection channel, a long pass filter with cut-on wavelength at 380 nm was used, so that the expected BV^- luminescence is supposed to be transmitted.

III. RESULTS AND DISCUSSIONS

A. EPR identification of BV^- center

Figure 2(a) shows a typical EPR spectrum of N and B codoped HPHT diamonds, named "plate-I" and "plate-II." This spectrum was obtained by a RP-EPR measurement [33,42,43], which focuses on low-concentration paramagnetic centers with long spin relaxation times. Major and minor paramagnetic centers in the crystals were neutral substitutional nitrogen (N_s^0 or the *P*1 center, $S = 1/2$) [53,54] and the NV^- center ($S = 1$) [39,45], respectively. When magnifying the NV^- EPR spectrum, another spin-1 center can be observed besides the low- and high-field-side NV^- signals, as shown in Figs. 2(b) and 2(c). This novel EPR signal originates from the BV^- center, showing a fourfold HF structure due to a ^{11}B nuclear spin ($I = 3/2$). Its concentration was estimated to be 1.5–2 ppb.

In Fig. 3, the spin-1 systems of the BV^- and NV^- centers are examined as a function of the magnetic-field angle θ. The definition of θ and the corresponding experimental coordinate are shown in Fig. 3(a) . As is clear in Fig. 3(b), both spin-1 systems are quite similar, displaying very similar zero-field splittings and the same C_{3v} symmetry ($\langle 111\rangle$-axial symmetry). Solid lines for NV^- were simulated using the known SH parameters of NV^- [39]. By analogy, solid lines for BV^- were also calculated using the SH parameters determined in this study. The SH parameters for the spin-1 BV^- and NV^- centers are defined by the following SH [55]:

$$H = \mu_B \boldsymbol{B}^{\mathrm{T}} \cdot \mathbf{g} \cdot \boldsymbol{S} + \boldsymbol{S}^{\mathrm{T}} \cdot \mathbf{D} \cdot \boldsymbol{S} + \boldsymbol{I}^{\mathrm{T}} \cdot \mathbf{A} \cdot \boldsymbol{S},$$

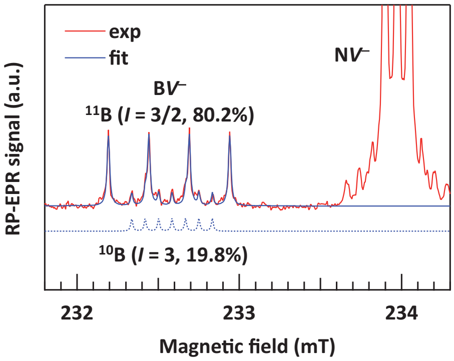

FIG. 4. Hyperfine (HF) interactions of ^{10}B and ^{11}B in the BV^- center, which generate fourfold and sevenfold HF splittings, respectively. A fitted curve was calculated by a combination of fourfold and sevenfold HF split structures with the given natural abundances. The RP-EPR spectra was recorded by using a field-modulation amplitude of 0.002 mT, microwave power of 0.2 mW, and an accumulation period of 16 000 s.

where μ_{B} is the Bohr magneton, ***B*** is a magnetic field vector (superscript "T" denotes a transposed vector), **g** is an electron gyromagnetic tensor (g tensor), ***S*** is an electron-spin operator, **D** is an electron spin-electron spin interaction tensor (D tensor), ***I*** is a nuclear-spin operator for ^{14}N or ^{10,11}B, and **A** is a hyperfine (HF) interaction tensor (A tensor). We omitted a nuclear Zeeman term and a nuclear quadrupole interaction term because they did not explicitly appear within the present angular-map analyses. By giving ***B***, **g**, **D**, and **A**, we numerically simulated the above SH by using an "EPR-NMR" SH simulator [56]. Since the spin-1 system of BV^- shows a C_{3v} symmetry ($\langle 111\rangle$-axial symmetry), its **g**, **D**, and **A** tensors can be determined from a pair of EPR spectra shown in Figs. 2(b) and 2(c). At $\theta = 54.75^\circ$ and 35.25°, one can directly find principal values of each tensor (e.g., $D_{//}$ and $D_\perp$ for the D tensor) parallel to and perpendicular to the symmetry axis, respectively. The determined SH parameters are summarized in . Solid lines for BV^- in Fig. 2(b) were simulated using these SH parameters.

The zero-field splitting constant D for BV^- is obtained to be $D = 3D_{//}/2 = 2913$ MHz, which is close to those of NV^- (2872 MHz) [39,45] and OV^0 (2888 MHz) [33]. This excellent consistency indicates that all these centers establish the common spin-1 system with the e_x and e_y levels as shown in Fig. 1. Previous first-principles calculations predicted consistent values of D for NV^- (2848 MHz) [35] and OV^0 (2989 MHz) [35], but a much smaller value for BV^- ($D = 1882$ MHz) [32]. The former two values were obtained using a 512-atom supercell [35], while the latter value for BV^- was calculated using a 64-atom supercell [32].

We further evidence the presence of a single boron atom in the BV^- center, which is shown in Fig. 4. In addition to the fourfold HF splitting due to ^{11}B ($I = 3/2$, natural abundance = 80.2%) in the BV^- spectrum, there is a weak sevenfold HF splitting, which arises from HF interactions with a ^{10}B nuclear spin ($I = 3$, natural abundance = 19.8%). In fact, as is shown in the figure, the experimental spectra can be fitted by a combination of ^{10}B and ^{11}B HF structures with their

TABLE I. SH parameters of the BV^- center in comparison with the known parameters of the NV^- and OV^0 centers. Principal values of **D** and **A** are expressed in MHz.

	g tensor (**g**)		D tensor (**D**)		A tensor (**A**)			
Spin-1 system	$g_{//}$	$g_{\perp}$	$D_{//}$	$D_{\perp}$	nuclear spin	$A_{//}$	$A_{\perp}$	Ref.
BV^-	2.0030	2.0038	1942.1	−971.0	^{11}B ($I = 3/2$)	7.0	5.5	this work
					^{10}B ($I = 3$)	2.3	1.9	
NV^-	2.0029	2.0031	1914.66	−957.33	^{14}N ($I = 1$)	−2.17	−2.63	Ref. [39]
OV^0	2.0029	2.0026	1925.3	−962.7				Ref. [33]

natural abundances. The principal HF constants ($A_{//}$ or $A_{\perp}$) for ^{10}B are 1/3 of those for ^{11}B (Table I). This factor simply coincides with the ratio (1/2.98) of their nuclear g factors ($g_n = 0.602\,20$ for ^{11}B $/g_n = 1.792\,437$ for ^{10}B).

When the magnetic field is apart from the principal-axis directions, the fourfold split ^{11}B HF structure further splits into more than five lines. This is due to a nuclear quadrupole interaction. The determination of the nuclear quadrupole interaction for BV^- will be saved for future work.

B. Boron hyperfine interaction of BV^- center

For a ^{11}B atom, isotropic and anisotropic HF constants, a and b, are known to be $a = 2547$ MHz and $b = 63.64$ MHz, respectively [55]. The experimental isotropic and anisotropic ^{11}B HF couplings, $A_{\text{iso}} = (A_{//} + 2A_{\perp})/3$ and $A_{\text{aniso}} = (A_{//}–A_{\perp})/3$ [55], are estimated to be 6.2 and 0.65 MHz, respectively. Within a simple linear combination of atomic orbitals (LCAO) approximation, A_{iso} and A_{aniso} should originate from 2s- and 2p-orbitals of an electron spin on a ^{11}B site. Thus, the ^{11}BV^- center has 2s-orbital fractions of $|A_{\text{iso}}/a| = 0.2\%$ and 2p-orbital fractions of $|A_{\text{aniso}}/b| = 1.0\%$ on its boron atom. These very small fractions ensure that the spin-1 system consists of carbon orbitals (the e_x and e_y states) on the vacancy side, supporting the picture in Fig. 1(c). This nature is exactly common to the case of the NV^- center [57].

Considering the symmetry for both BV^- and NV^-, a dangling bond of each impurity atom should not be mixed into their e state. In fact, the wave function of NV^- is mostly localized on three C atoms, and its remainder spreads over other far C atoms mostly in the plane perpendicular to the N-V axis [57]. The very weak boron HF interactions point towards a similar situation for the BV^- center. In such a case, the anisotropic part of the HF interaction (A_{aniso}) can be mainly contributed by a dipolar interaction between an impurity's nuclear spin and an electron spin on other atoms. Actually, in the NV^- center, the observed anisotropic part, $A_{\text{aniso}} = 0.19$ MHz, agrees with the dipolar interaction (0.18 MHz) between a ^{14}N nucleus and spin densities on three nearest-neighbor C atoms calculated with N-C = 2.51 Å [39]. If we replace the ^{14}N nucleus ($g_n = 0.403\,763\,7$) with the ^{11}B nucleus ($g_n = 1.792\,437$), the dipolar interaction of $0.18 \times 1.7924/0.403\,76 = 0.80$ MHz is estimated with the same symmetrical axis, which is similar to the observed A_{aniso} value (0.65 MHz). This also supports the correspondence between BV^- and NV^-.

C. Optically induced spin polarization of BV^- center

One of the greatest advantages of the NV^- center is its spin-selective optical responses, which are crucial in spin polarization and readout of its spin qubit. With an optical pumping at ∼532 nm, the triplet spin system of NV^- can be polarized into the $m_S = 0$ state via a spin-dependent branching path in the decay process depicted in Fig. 5(a). After a strong spin polarization as shown in the diagram of Fig. 5(b), pairs of absorption and emission lines are observable at the low- and high-field sides, respectively, and simultaneously EPR signal intensities are enhanced. Such a spin-polarization behavior was absent for the spin-1 OV^0 center [33–35]. In contrast, the spin-1 BV^- center clearly shows the spin-polarization behavior, which appears in the high-field-side spectra in Fig. 5(c). For this experiment, we used a white light (150-W xenon lamp) + band-pass filters (365 ± 15 nm). Unfortunately, optical responses of BV^- were not intense at room temperature, due to a weak filtered light (<1 mW). Within this setup, the spin polarization was almost absent even for the NV^- center. However, at lower temperatures, the spin polarization became stronger for both the NV^- and BV^- centers. Eventually, at 150 K or lower. we clearly detected enhanced high-field-side emission lines (also enhanced low-field-side absorption lines) for BV^-, demonstrating its optically induced spin polarization. When we used an optimized wavelength for NV^- (e.g., 530 nm), its spin polarization was further strongly enhanced.

The optical spin polarization loop of NV^- originates from its four-level structure consisting of the $^3A_2$, ^3E, $^1A_1$, and ^1E states [Fig. 5(a)]. Spin-selective intersystem crossing (ISC) from ^3E to $^1A_1$ caused by the phonon-mediated spin-orbit coupling is crucial in its efficient optical spin polarization [58,59]. First-principles calculations on BV^- predicted the spin-conserving transition from a $^3A_2$ triplet ground state to a ^3E triplet excited state; however, its intermediate singlet states were not calculated [37,38]. Our observation indicates that the BV^- center has intermediate singlet state(s), common to the NV^- system.

We further studied optical thresholds of the BV^- and coexisting NV^- centers by means of photo-EPR spectroscopy [47,48]. Figures 6(a) and 6(b) show sets of photo-EPR spectra for NV^- and BV^-, respectively, in the energy range between 0.50 and 5.50 eV. In Fig. 6(a), we can find the established optical responses of the NV^- center [62]. The spin polarization of NV^- was observable in the range between 1.95 and 2.25 eV (636 and 551 nm), where the low- and high-field-side NV^-

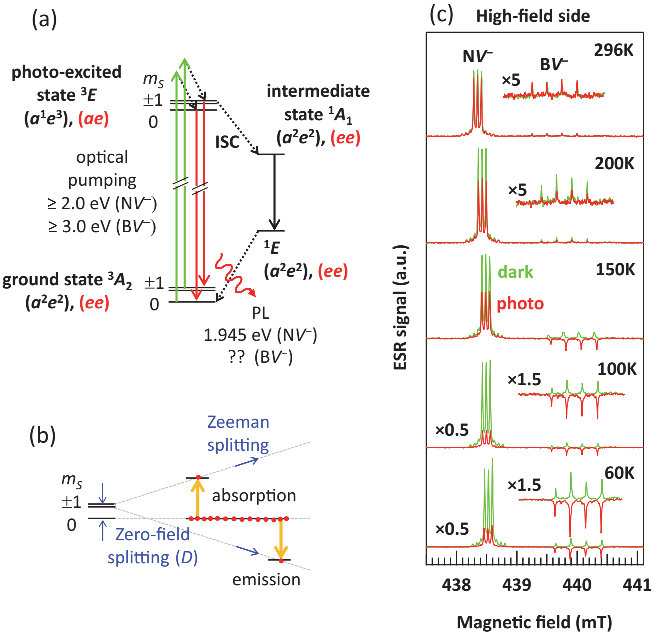

FIG. 5. (a) Optical spin-polarization loop of NV^-. Electronic configurations corresponding to $^3A_2$, ^3E, $^1A_1$, and ^1E are shown in terms of electron representation (black) and hole representation (red) [60,61]. For instance, $(a_1)^2e^2$ and $(a_1)^1e^3$ for $^3A_2$ and ^3E in the electron representation are rewritten as (ee) and (ae) in the hole representation, respectively. Intermediate states of $^1A_1$ and ^1E are assigned to (ee) in the hole representation. Likewise NV^- system, $^3A_2$ ground state and ^3E excited state of BV^- are assigned to (ee) and (ae) in the electron representation, respectively. We assumed that BV^- has a similar four-level scheme, judging from its spin-polarization behavior similar to that of NV^-. Their ground and photoexcited states commonly have triplet spin states with $m_S = -1, 0, +1$. Green line expresses an optical pumping from the ground $^3A_2$ state to the excited ^3E state. For NV^-, the optical-pumping threshold is 1.945 eV [1,45], and that of 3.0 eV for BV^- was determined in this study. The photoexcited state is decayed into the ground state via two pathways: a PL emission (red line) or a nonradiative decay via an intermediate state (black lines). The latter process converts $m_S = \pm 1$ states into an $m_S = 0$ state, causing spin polarization such that the $m_S = 0$ state has a nonequilibrium large population. The PL line of NV^- appears at 1.945 eV, while that of BV^- is still unclear. (b) Spin polarization of the $m_S = 0$ level via optical pumping, which generates a high-field-side emission line in the EPR spectrum. (c) Temperature dependence of spin polarization seen in high-field-side EPR spectra before and after optical pumping by a filtered light of 365 ± 15 nm (3.40 ± 0.15 eV). Light power was ~1 mW just at the end of a fiber guide. The actual power at the sample was rather decreased due to a transmission loss from fiber end to microwave cavity. Due to spin polarization, low-field-side lines can be enhanced, while high-field-side lines can be reduced or reversed, as shown here.

signals revealed nonequilibrium signal intensities due to the optical pumping [see also Fig. 6(c)]. This range covers the optimal excitation wavelength (510–540 nm) for studying the NV^- luminescence. Above this range, the spin polarization of NV^- was canceled because the single-photon ionization of NV^- to NV^0 started (ionization threshold = 2.6 eV) [62]. Further increasing the excitation energy up to 2.9 eV, the NV^- center reexhibited the spin polarization. This threshold is consistent with the known recombination energy of 2.94 eV, causing the recovery of NV^0 to NV^- states [62].

Likewise, in Fig. 6(b), we also found a clear signature of the spin polarization for BV^- in the range between 3.0 and 3.6 eV (413 and 344 nm), where the high-field-side emission lines are observed. The optical pumping may start from ~2.8 eV for BV^- [cf., Fig. 6(c)], above which it can start an optical transition from a triplet ground state to a triplet excited state. This threshold is similar to a calculated ZPL (3.22 eV) of the spin-conserving transition of BV^- [38].

Above 3.7 eV, the BV^- signal was quenched, suggesting that the single-photon ionization energy of BV^- ($BV^- + h\nu \rightarrow BV^0 + e^-{}_{\rm CB}$) is 3.7 eV. Thus, the ground state of BV^- is supposedly located at around $E_{\rm C}$–3.7 eV ($E_{\rm V}$ + 1.8 eV). This valence-band-side level matches the calculated (−/0) levels of BV: $E_{\rm V}$ + 1.5–1.6 eV [32,37,38], supporting our identification from the viewpoint of energy levels.

We also observed other optical quenching in the range between 1.4 and 2.3 eV (886 and 539 nm) for BV^-. These thresholds may be related to charge transfers between BV^- and the valence band or other charge traps including in the specimen. Further works are required to elucidate the origins of these thresholds.

It is also noted that we have not detected an EPR signal of BV^0 ($S = 1/2$) in the photo-EPR experiments. The absence of the spin-1/2 center is ascribed as a signal-broadening mechanism just the same as the case of the NV^0 center ($S = 1/2$) [46].

D. Optical and EPR imaging on N and B codoped diamonds

First-principles calculations indicate that the charge state of the BV center varies with the Fermi level ($E_{\rm F}$) such as BV^+ ($E_{\rm F}$–$E_{\rm V}$ < 0.6 eV [38] or $E_{\rm F}$–$E_{\rm V}$ < 1.2 eV [37]), BV^0 (0.6 < $E_{\rm F}$–$E_{\rm V}$ < 1.6 eV [38] or 1.2 < $E_{\rm F}$–$E_{\rm V}$ < 1.5 eV [37]), BV^- (1.6 < $E_{\rm F}$–$E_{\rm V}$ < 3.6 eV [38] or 1.5 < $E_{\rm F}$–$E_{\rm V}$ < 2.7 eV [37]), and BV^{2-} ($E_{\rm F}$–$E_{\rm V}$ > 3.6 eV [38] or $E_{\rm F}$–$E_{\rm V}$ > 2.7 eV [37]). Thus, we expect that the BV^- center is stable with $E_{\rm F}$ in the midgap range. Since the neutral boron has an acceptor level at $E_{\rm V}$ + 0.37 eV [63], B-doped diamonds after irradiation may form the BV^+ and/or BV^0 centers predominantly. To create BV^- associated with a proper $E_{\rm F}$, N and B codoping may be necessary. In this section, we conclude that the BV^- centers are preferentially formed in {111} growth sectors, which are revealed by EPR imaging and luminescence microscopy.

Figure 7(a) illustrates the preparation of a diamond plate (plate-II) from a HPHT crystal. Typical HPHT crystals have a habit of cubo-octahedron consisting of as-grown {100} and {111} facets. Internal morphology exhibits growth sectors, which show different uptake rates for impurities, since different growth sectors have different growth planes and different growth rates [64]. Therefore, the concentrations of N and B should be inhomogeneous in the plate, which is the key for creating BV^-. The distribution of the growth sectors is clearly seen in the "DiamondView" image shown in Fig. 7(b). The DiamondView provides a fluorescence image under excitation of UV at wavelengths shorter than ~230 nm from a filtered xenon arc lamp source. The DiamondView image only reveals a near-surface information, because of the short penetration depth of the UV light. In Fig. 7(b), the {100} growth sectors

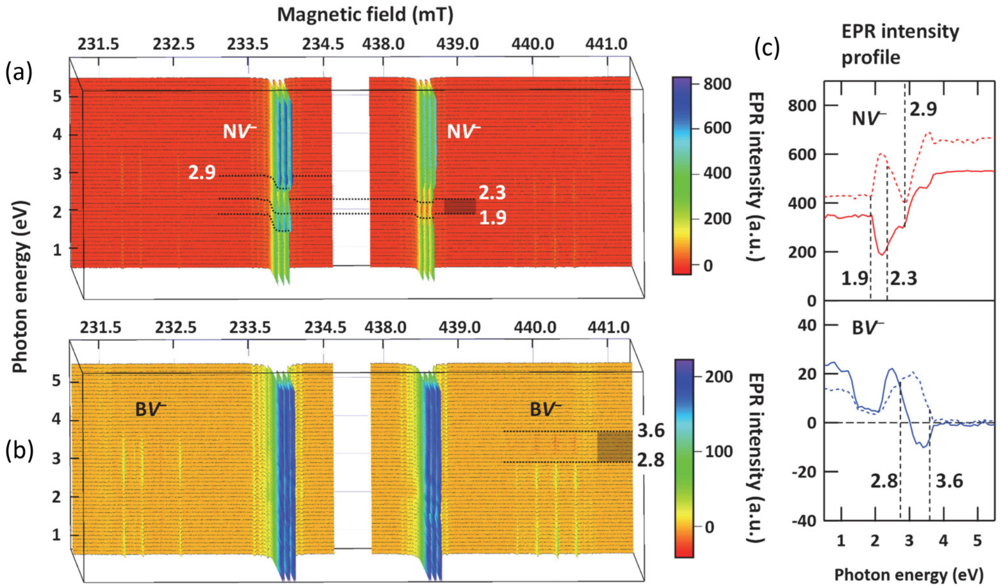

FIG. 6. Photo-EPR measurements on BV^- and NV^- centers at 60 K for $\boldsymbol{B}$ // [111]. Light power was 5–10 μW at the end of a fiber guide. Highlighted parts in (a) and (b) indicate optical pumping ranges for spin polarizations of NV^- and BV^-, respectively. Most outer weak resonances in (b) arise from ^{13}C HF satellites of NV^-. (c) EPR intensity profiles of NV^- and BV^- centers (averaged intensities of their threefold-split and fourfold-split lines, respectively). Solid and dashed lines are calculated using high-field-side and low-field-side lines, respectively. Optical thresholds are also indicated.

(at a center of both faces and four corners of seed-side face) show bright red fluorescence, indicating the formation of the NV centers (NV^- and NV^0). In contrast, four {111} growth sectors surrounding the central {100} sector appear as darker areas, suggesting low NV concentrations. Our samples consist predominantly of {100} and {111} growth sectors together with very minor {113} and {110} sectors. Since these sectors show different impurity concentrations, our plate is like an inhomogeneous semiconductor. Therefore, for each sector, the E_F position relative to E_V can vary with its impurity concentration.

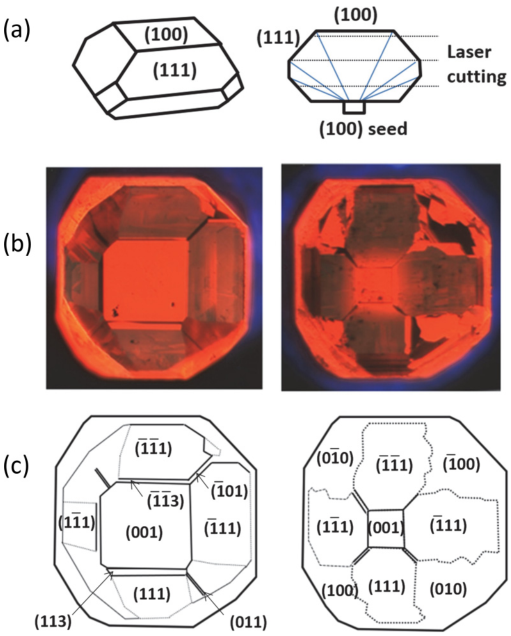

FIG. 7. Growth sectors in N and B codoped diamond. (a) Preparation of a (100) diamond plate for EPR imaging and PL/CL study. Plate-II (1.34 mm thick) was cut out from the upper middle of a HPHT crystal by laser-cutting. (b) A "DiamondView" image of the plate. Image of the seed-side face (right) is mirrored to make the view direction the same as that of the growth-side face (left). Brighter and darker areas indicate {100} and {111} growth sectors, respectively.

Using optical microscopy and EPR imaging (Fig. 8), we further reveal the charge states of N and B impurities and examine the relative E_F positions in these growth sectors. From CL microscopy shown in Figs. 8(c) and 8(d), the concentration of neutral boron acceptor [$\mathrm{B_s}^0$] is determined for each sector from the intensity ratio of excitonic recombination assisted by a transverse optical (TO) phonon between the neutral-boron bound exciton (BE) and the free exciton (FE) [65,66]. In the {111} growth sectors, [$\mathrm{B_s}^0$] estimated from the ratio of $\mathrm{BE_{TO}/FE_{TO}}$ are 6.4×10^{16} cm^{-3} (0.36 ppm) and 7.2×10^{16} cm^{-3} (0.41 ppm) at positions 3 and 4, respectively. On the contrary, in the {100} growth sectors, [$\mathrm{B_s}^0$] was below the detection limit. The concentration of $\mathrm{N_s}^0$ is also estimated from the optical absorption band at 270 nm at room temperature [67]. The [$\mathrm{N_s}^0$] of the {100} and {111} growth sectors of plate-II obtained from the UV absorption are 1.4 ppm and below 0.1 ppm (detection limit), respectively.

The EPR imaging visualizes two-dimensional spatial distributions of $\mathrm{N_s}^0$ and the NV^- center in the plate, which are shown in Figs. 8(a) and 8(b), respectively. EPR imaging reveals that both $\mathrm{N_s}^0$ and NV^- are preferentially present in the {100} growth sectors. Neutral nitrogen $\mathrm{N_s}^0$ has a deep donor level at E_C–1.7 eV (E_V + 3.8 eV) [68]. The ground state of NV^- is located at E_C–2.6 eV (E_V + 2.9 eV) [69]. Thus, the Fermi level in the {100} growth sectors should be higher than the midgap (E_C–2.8 eV or E_V + 2.7 eV). PL microscopy

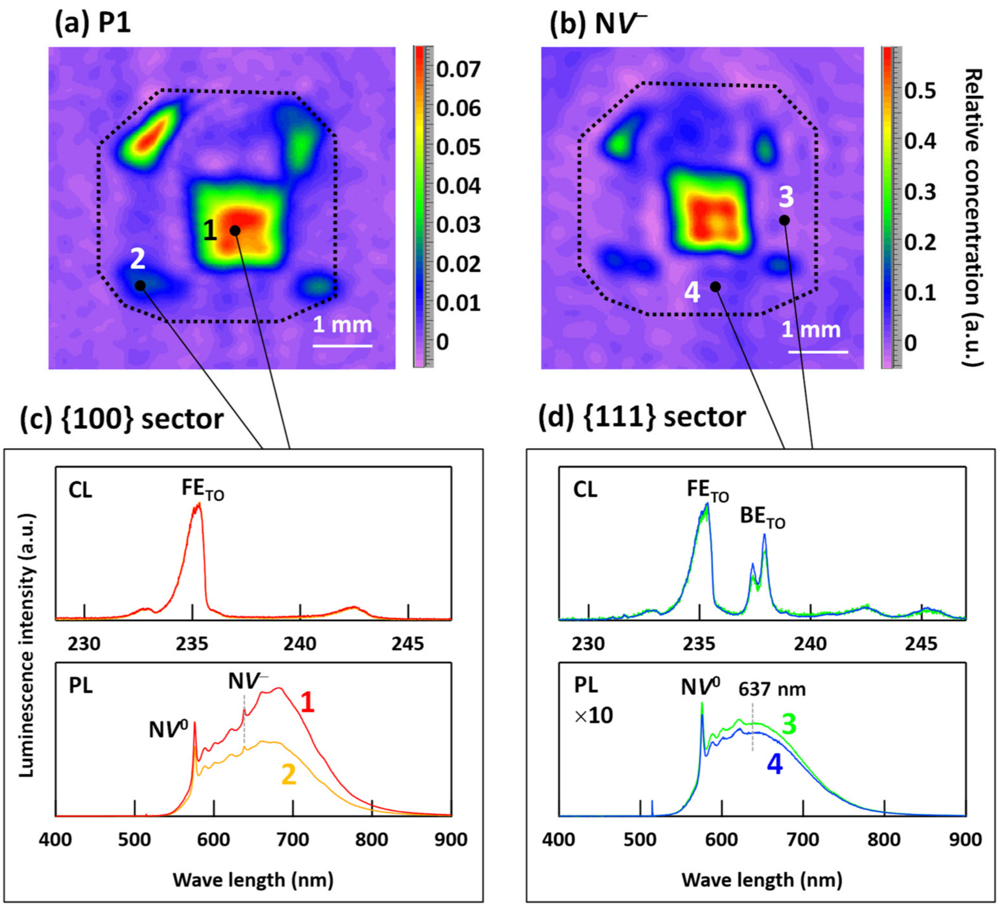

FIG. 8. Two-dimensional EPR imaging of (a) *P*1 distribution and (b) NV$^-$ distribution. Both *P*1 and NV$^-$ are revealed to be dominantly distributed in the {100} growth sector. NV$^-$ distribution was recorded under 532-nm optical excitation. (c), (d) Room-temperature PL spectra using 514.5-nm excitation and CL spectra at 83 K obtained for {100} and {111} growth sectors, respectively. In CL spectra, luminescence from a neutral-boron bound exciton (BE$_{\rm TO}$) was only observed for the {111} growth sector. These CL spectra were normalized by each free-exciton luminescence (FE$_{\rm TO}$) intensity. PL spectra indicate that a nitrogen vacancy exists in the {111} growth sector, mostly in the form of the NV^0 center (ZPL: 575 nm).

[Fig. 8(c)] supports the presence of NV^0 and NV^-, which appears as zero phonon lines (ZPLs) at 575 and 637 nm, respectively [1]. Judging from these observations, we expect that a dominant charge state is BV^{2-} if the B*V* centers were formed in this sector.

Furthermore, we suggest that they are barely formed in the {100} sectors, because of low boron concentration. It is already known that $[{\rm B_s}^0]_{\{111\}} > [{\rm B_s}^0]_{\{110\}} > [{\rm B_s}^0]_{\{113\}} > [{\rm B_s}^0]_{\{100\}}$ for B-doped diamonds [64,70], where the suffix of {*hkl*} refers to the {*hkl*} growth sector. Accordingly, the boron incorporation is normally much less (∼1/100) in the {100} sectors than in the {111} sectors [70,71], reducing the number of B*V* in the {100} sectors of our crystal.

In contrast with the {100} growth sectors, the {111} sectors expectedly generate the BV^- center after the electron irradiation and subsequent annealing, as described below. First, a much larger uptake of boron (the BE$_{\rm TO}$ peak) is evidenced by CL microscopy [Fig. 8(d)], which detected ${\rm B_s}^0$ of ∼0.4 ppm. On the other hand, the EPR imaging [Fig. 8(a)] and the optical absorption reveal the absence of ${\rm N_s}^0$, although it is generally known that $[{\rm N_s}^0]_{\{111\}} > [{\rm N_s}^0]_{\{100\}} > [{\rm N_s}^0]_{\{113\}} > [{\rm N_s}^0]_{\{110\}}$ [64]. We deduce that the absence of ${\rm N_s}^0$ is mainly due to the B-doping. Nitrogen and boron impurities compensate each other:

$$ {\rm N_s}^0 + {\rm B_s}^0 \rightleftarrows {\rm N_s}^+ + {\rm B_s}^-. $$

Adding boron impurities changes ${\rm N_s}^0$ into ${\rm N_s}^+$ ($S = 0$). Moreover, it was reported that the ratio of $[{\rm N_s}^0]$ between the {111} and {100} sectors depends on the growth temperature [72]. At a low growth temperature, $[{\rm N_s}^0]$ in the {111} sectors became lower (∼0.76 times) than in the {100} sectors. With these factors, ${\rm N_s}^0$ are absent in the {111} sectors of our sample. The PL spectra [Fig. 8(d)] indicate that the N*V* centers are mostly in the NV^0 state, suggesting a lower $E_{\rm F}$ in the {111} sectors. First-principles calculations estimated that the NV^0 state is stable when $1.1 < E_{\rm F}–E_{\rm V} < 2.6\,{\rm eV}$ [69]. This range overlaps with the range in which the BV^- state is stable. Thus, the $E_{\rm F}$ position of the {111} sectors is most probably tuned to stabilize the BV^- state (stable when $E_{\rm F}–E_{\rm V} > 1.6\,{\rm eV}$) [37,38] via N and B codoping.

It might be puzzling that ${\rm B_s}^0$ (the acceptor level of $E_{\rm V} + 0.37\,{\rm eV}$) and BV^- coexisted in the {111} sectors of our sample. In diamond, it was pointed out that a defect charge state is not uniquely determined by the Fermi level [73]. As a result, two different charge states of the same defect can coexist in a single crystal. When impurity concentrations are

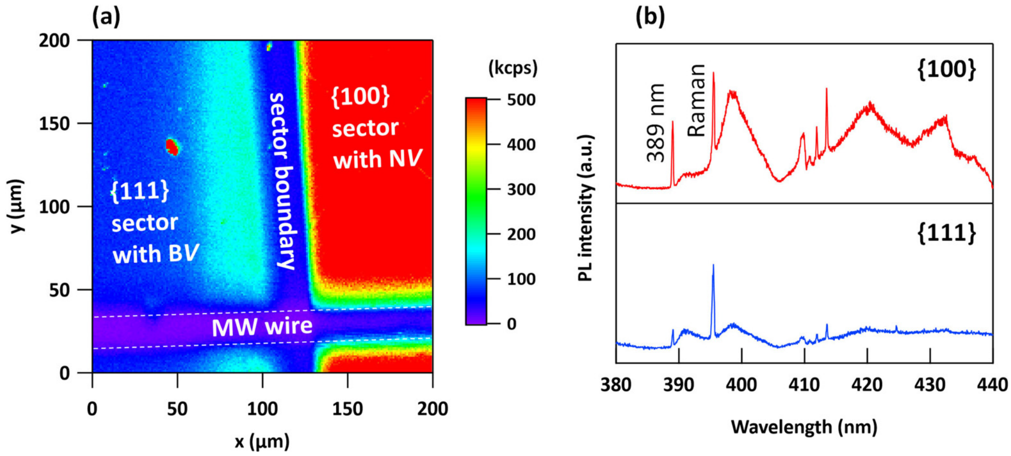

FIG. 9. (a) Confocal microscope image of N and B codoped diamond. "MW wire" is used for microwave radiation when ODMR is recorded. The excitation wavelength was 375 nm, which can generate triplet-to-triplet excitation and spin polarization for BV^-. In the {100} growth sectors, a strong luminescence was observed due to ensemble NV^- centers, while in the {111} sectors, no strong luminescence was detected in spite of the presence of BV^-. (b) Typical PL spectra from {100} and {111} growth sectors (acquisition times are the same). In the region around 414 nm, luminescence from the {100} area remains stronger compared to the {111} area. Peak intensity of the 389-nm line is ~1/50 times smaller than that of the 575-nm line of NV^0 under 375-nm excitation. The 389-nm center is a nitrogen-related radiation-induced defect. Sharp peaks around 412 nm are likely to be local mode replicas of 389-nm ZPL [74].

$<$ 10 ppm, the distance between a defect and a donor (or an acceptor) has a wide variation. The charge state of a defect depends on such a distance [73]. Accordingly, the coexistence of $B_s{}^0$ and BV^- becomes possible in the {111} sectors of our crystals.

E. CFM imaging

As was shown in Sec. III C, the BV^- center allows the triplet-to-triplet optical excitation above ~2.8 eV, leading to the spin polarization. We tried to identify PL of this center using a 375-nm (3.3-eV) excitation laser in a special low-temperature CFM apparatus. We note again that this excitation wavelength fits with the calculated ZPL of BV^- (3.22 eV or 385 nm) [38] as well as with the beginning of a *strong* spin polarization observed in our photo-EPR studies (threshold ~ 3.0 eV).

Figure 9(a) shows a typical CFM raster scan obtained at 4 K with a 380-nm-long pass filter, visualizing the border of the {111} and {100} growth sectors. As discussed above, the {100} sector contains a much higher concentration of the NV centers, resulting in much brighter luminescence. However, even restricting the detection window to the region of 390–440 nm, the {100} growth sector remains brighter as indicated in Fig. 9(b), due to the appearance of the 389-nm line and its replicas [74]. The spectrum obtained from the {111} area did not exhibit any specific features assignable to the BV^- luminescence. Moreover, we applied a microwave field swept in the range of 2–3 GHz under constant 375-nm illumination, trying to observe optically detected magnetic resonance (ODMR). Limiting the detection window from 391 to 450 nm, we could not observe ODMR either from the {111} or {100} area. As a control measurement, using a 532-nm excitation laser and detecting light from the {100} sector with a 650-nm-long pass filter, an ODMR signal corresponding to the NV^- centers was instantly observed. At present, we conclude that the luminescence from the BV^- center is much weaker compared to the NV^- center.

Although the three centers, NV^-, OV^0, and BV^-, exhibit a close similarity in their ground states ($^3A_2$), quite different decays are observed from their photoexcited states. We deduce that such a difference originates mainly from the nature of their excited states (^3E). The $^3A_2$ ground state is an orbital singlet that is not subject to the Jahn-Teller distortion. On the other hand, the ^3E triplet excited state, which is Jahn-Teller unstable, originates from different electronic configurations for the three centers: $(a_1)^1e^3$ for NV^-, $e^1(3a_1)^1$ for OV^0, and $e^1(a_1)^1$ for BV^-. In the NV^- center, an electron is excited from a_1 into the e level which consists of pure carbon orbitals (see Appendix A). At room temperature, the excited state of NV^- maintains the C_{3v} symmetry, since NV^- is a dynamic Jahn-Teller system with a small barrier energy of reorientation [1]. In the case of OV^0, an electron is promoted from the e state to the antibonding $3a_1$ state of C-O bonds with three back-bonded carbon atoms (Appendix A). From the ^3E excited state of OV^0, a very fast nonradiative decay leads to a metastable state (C_s symmetry) with a reconstructed structure having two C-O covalent bonds and one elongated C-O bond [35]. The symmetry lowering from C_{3v} to C_s is the outcome of the Jahn-Teller distortion. As a result, OV^0 is expected to have a very weak or no luminescence [35]. In the case of BV^-, an electron is promoted from the e state to the a_1 state, which is high in energy due to a large involvement of the dangling bond of boron less electronegative than carbon [32,38]. It may result in a large Jahn-Teller distortion for BV^-. Accordingly, a different manifestation of the Jahn-Teller effect and the spin-orbit coupling may be expected for BV^- as compared to the NV^- system. The exact influence on the BV^- luminescence by such factors remains an open question, and will be clarified via sophisticated first-principles calculations in the future. The theoretical studies will also help us to understand an association between the weak luminescence and the spin polarization.

IV. SUMMARY

We have found a novel EPR center of BV^- in N and B codoped diamonds. Our EPR identification showed that the BV^- center has a very similar triplet ground state ($S = 1$, C_{3v} symmetry, and $D = 2913$ MHz) to the NV^- center ($S = 1$, C_{3v} symmetry, and $D = 2872$ MHz). The involvement of a single boron atom was evidenced by its HF interaction due to ^{10}B or ^{11}B nuclear spin.

Furthermore, we confirmed that the triplet-to-triplet optical excitation with the threshold of ~3.0 eV (413 nm) produces the spin polarization for this center. This optical-pumping behavior was similar to the NV^- center, and was apart from another analog center of OV^0 ($S = 1$, C_{3v} symmetry, and $D = 2888$ MHz). However, unlike the NV^- center, the BV^- center did not show detectable luminescence after the triplet-to-triplet optical excitation even at low temperatures (e.g., 4 K). Accordingly, we have not yet identified PL from the BV^- centers. At least, our experimental results indicated that, among the three analog centers of NV^-, OV^0, and BV^-, only the NV^- center is an extraordinary luminescent center. Understanding the reason why the BV^- luminescence is strongly weakened remains a future work.

For creating the BV^- center, it is the key to tuning the Fermi level to a specific position by taking advantage of N and B codoping. We demonstrated using a combination of optical microscopy and EPR imaging that inhomogeneous impurity distributions in N and B codoped diamonds make it possible to create the BV^- center preferentially within the {111} growth sectors.

ACKNOWLEDGMENTS

This work was carried out as a joint project of University of Tsukuba, Ulm University, and University of Stuttgart. This work was partly supported by the Japan Society of the Promotion of Science (JSPS) KAKENHI, Grants No. JP20H00340, and K.W. was supported from JSPS KAKENHI Grant No. JP17H02748. J.W. acknowledges support by the Max Planck Society, the EU via ERC grant SMeL, and the project QIA and ASTERIQS as well as the DFG via FOR 2724. F.J. acknowledges support by EU via ERC and projects ASTERIQS and HYPERDIAMOND, DFG, BMBF, and VW Stiftung. P.S. acknowledges Baden-Württemberg Stiftung for the financial support via Eliteprogramme for Postdocs.

APPENDIX A: A SIMPLE MODEL ON ELECTRONIC STATES OF NV^-, OV^0, AND BV^-

Using a simple defect-molecule model consisting of an impurity atom X (= N, O, and B) and three carbon atoms (C$_1$, C$_2$, and C$_3$) surrounding a vacancy, molecular orbitals (MOs) of one-electron states are given by a linear combination of atomic orbitals (LCAO) of four dangling-bond orbitals (σ_X, σ_1, σ_2, and σ_3). Under the C_{3v} symmetry, four MOs are derived:

$$a_1{}' = \sigma_X - \lambda'(s_1 + s_2 + s_3),$$

$$a_1 = (\sigma_1 + \sigma_2 + \sigma_3) + \lambda\sigma_X,$$

$$e_x = 2\sigma_1 - \sigma_2 - \sigma_3,$$

$$e_y = \sigma_2 - \sigma_3,$$

where λ and λ' are LCAO coefficients [1]. In the NV^- and OV^0 centers, the $a_1{}'$ and $1a_1$ MO approximately expresses a nitrogen lone pair and an oxygen lone pair, respectively [see Figs. 1(a) and 1(b)], since nitrogen and oxygen are more electronegative than carbon. On the other hand, the a_1 and $2a_1$ MO approximately expresses a combination of three carbon dangling bonds.

Since boron is less electronegative than carbon, a boron-related a_1 state in the BV^- center is energetically located much higher than the e_x and e_y states [Fig. 1(c)], contrary to the cases of NV^- and OV^0 [32]. First-principles calculation predicted that the unoccupied a_1 state located higher in the band gap originates mainly from a boron dangling bond [37,38].

In the OV^0 center, there is an unoccupied a_1 state labeled "$3a_1$" [Fig. 1(b)] in the upper side of the band gap, in addition to the vacancy-related states [32,35]. The $3a_1$ MO is an antibonding orbital of oxygen and three back-bond carbon atoms [32,35].

All three centers have a common triplet ground state ($S = 1$, $^3A_2$ many-electron state) arising from two parallel-spin electrons occupying doubly degenerate e orbitals. The two e orbitals (e_x and e_y) consist of pure carbon orbitals, as is seen in the above relations.

APPENDIX B: COHERENCE TIME AND ENGINEERING CONSIDERATION OF BV^-

We expect that the coherence time of BV^- can be engineered to be as long as that of NV^-. The long coherence time of NV^- benefits from the uniqueness of diamond [1]. The high Debye temperature and weak spin-orbit coupling extremely elongate the spin-lattice relaxation time (T_1) of NV^-. Secondly, the sources of local-field fluctuations can be extremely reduced by ^{12}C-isotope enrichment. BV^- can gain these benefits similarly to NV^-.

When NV^- is fabricated by a conversion between N and NV (via electron irradiation and subsequent annealing, etc.), residual substitutional nitrogen atoms, $\mathrm{N_s}^0$ ($S = 1/2$), play a major role in shortening the spin coherence times, $T_2{}^*$ and T_2, of NV^-. For example, our EPR imaging of Figs. 8(a) and 8(b) indicates such a situation. On the contrary, EPR imaging on the {111} sectors, where BV^- is fabricated, did not exhibit the $\mathrm{N_s}^0$ signal. Thus, the Fermi-level tuning creating BV^- makes a nonparamagnetic state of substitutional nitrogen, $\mathrm{N_s}^+$ ($S = 0$). Accordingly, the sources of local-field fluctuations were greatly reduced. Instead of $\mathrm{N_s}^0$, a low concentration of $\mathrm{B_s}^0$ ($S = 1/2$) is present in the {111} sectors. However, $\mathrm{B_s}^0$ having a short spin-lattice relaxation time is unlikely to shorten the coherence time of BV^-.

It should be noted that the EPR signal of BV^- was measured with a high sensitivity by using the RP-EPR technique. This technique is only effective in a paramagnetic species having a long relaxation time.

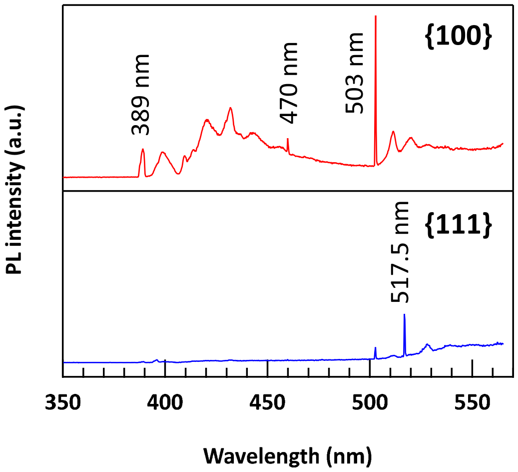

FIG. 10. Typical wide-range PL spectra measured with 375-nm excitation at 4 K from {100} and {111} growth sectors (acquisition times are the same).

It is also expected that BV^- has the same weak points as those of NV^-. The weak points of NV^- are as follows: (i) only ∼4% of the emission is extracted as a ZPL, and (ii) a lack of the inversion symmetry makes ZPL frequencies highly sensitive to local electric fields and local strain. These weaknesses add a non-negligible difficulty in applying NV^- to photon-spin interfaces and quantum communication. A similar weakness will be found for BV^-. In contrast with NV^- and BV^-, impurity-vacancy defects having D_{3d} symmetry such as SiV^- reveal a vanishing permanent electric dipole moment of the ground and excited states, which makes their optical transition insensitive to electric-field noise in nanostructures (e.g., in photonic cavity). For NV^-, however, nanostructures such as a solid immersion lens and a nanopillar are widely useful for enhancing the photon collection [75]. A similar strategy will also be useful for BV^- if its photoluminescence is visible.

APPENDIX C: WIDE-RANGE PL SPECTRA

The PL spectra shown in Fig. 9(b) were taken with the grating 1596 grooves/mm. PL spectra for a wide wavelength range taken with a lower resolution (grating 150 grooves/mm) are shown in Fig. 10. No PL features assignable to BV^- were observed in this range.

The center with ZPL at 470nm is "TR12" which is a radiation-induced center observed in all types of diamonds [76]. The PL feature with ZPL at 503 nm and a phonon replica of 41 meV arises from the H3 center, [N-V-N]^0, according to the literatures [e.g., [77]]. The PL with ZPL at 517.5 nm and a phonon replica of ∼51 meV was observed in boron-doped HPHT diamond crystal with the low nitrogen concentration [78].

[1] M. W. Doherty, N. B. Manson, P. Delaney, F. Jelezko, J. Wrachtrup, and L. C. L. Hollenberg, Phys. Rep. **528**, 1 (2013).

[2] M. V. G. Dutt, L. Childress, L. Jiang, E. Togan, J. Maze, F. Jelezko, A. S. Zibrov, P. R. Hemmer, and M. D. Lukin, Science **316**, 1312 (2007).

[3] P. Neumann, N. Mizuochi, F. Rempp, P. Hemmer, H. Watanabe, S. Yamasaki, V. Jacques, T. Gaebel, F. Jelezko, and J. Wrachtrup, Science **320**, 1326 (2008).

[4] F. Dolde, I. Jakobi, B. Naydenov, N. Zhao, S. Pezzagna, C. Trautmann, J. Meijer, P. Neumann, F. Jelezko, and J. Wrachtrup, Nat. Phys. **9**, 139 (2013).

[5] G. Waldherr, Y. Wang, S. Zaiser, M. Jamali, T. Schulte-Herbrüggen, H. Abe, T. Ohshima, J. Isoya, J. F. Du, P. Neumann, and J. Wrachtrup, Nature (London) **506**, 204 (2014).

[6] T. H. Taminiau, J. Cramer, T. van der Sar, V. V. Dobrovitski, and R. Hanson, Nature Nanotechnol. **9**, 171 (2014).

[7] C. E. Bradley, J. Randall, M. H. Abobeih, R. C. Berrevoets, M. J. Degen, M. A. Bakker, M. Markham, D. J. Twitchen, and T. H. Taminiau, Phys. Rev. X **9**, 031045 (2019).

[8] E. Togan, Y. Chu., A. S. Trifonov, L. Jiang, J. Maze, L. Childress, M. V. G. Dutt, A. S. Sørensen, P. R. Hemmer, A. S. Zibrov, and M. D. Lukin, Nature (London) **466**, 730 (2010).

[9] W. Praff, B. Hensen, H. Bernien, S. B. van Dam, M. S. Blok, T. H. Taminiau, M. J. Tiggelman, R. N. Schouten, M. Markham, D. J. Twitchen, and R. Hanson, Science **345**, 532 (2014).

[10] B. Hensen, H. Bernien, A. E. Dréau, A. Reiserer, N. Kalb, M. S. Blok, J. Ruitenberg, R. F. L. Vermeulen, R. N. Schouten, C. Abellán, W. Amaya, V. Pruneri, M. W. Mitchell, M. Markham, D. J. Twitchen, D. Elkouss, S. Wehner, T. H. Taminiau, and R. Hanson, Nature (London) **526**, 682 (2015).

[11] N. Kalb, A. A. Reiserer, P. C. Humphreys, J. J. W. Bakermans, S. J. Kamerling, N. H. Nickerson, S. C. Benjamin, D. J. Twitchen, M. Markham, and R. Hanson, Science **356**, 928 (2017).

[12] D. D. Awschalom, R. Hanson, J. Wrachtrup, and B. B. Zhou, Nat. Photon. **12**, 516 (2018).

[13] L. Rondin, J.-P. Tetienne, T. Hingant, J.-F. Roch, P. Maletinsky, and V. Jacques, Rep. Prog. Phys. **77**, 056503 (2014).

[14] R. Schirhagl, K. Chang, M. Lorentz, and C. L. Degen, Annu. Rev. Phys. Chem. **65**, 83 (2014).

[15] F. Casola1, T. van der Sar, and A. Yacoby, Nat. Rev. Mater. **3**, 17088 (2018).

[16] F. Dolde, H. Fedder, M. W. Dopherty, T. Nöbauer, F. Rempp, G. Balasubramanian, T. Wolf, F. Reinhard, L. C. L. Hollenberg, F. Jelezko, and J. Wrachtrup, Nat. Phys. **7**, 459 (2011).

[17] J. Michl, J. Steiner, A. Denisenko, K. Nakamura, H. Sumiya, S. Onoda, P. Neumann, J. Isoya, and J. Wrachtrup, Nano Lett. **19**, 4904 (2019).

[18] P. Neumann, I. Jakobi, F. Dolde, C. Burk, R. Reuter, G. Waldherr, J. Honert, T. Wolf, A. Brunner, J. H. Shim, D. Suter, H. Sumiya, J. Isoya, and J. Wrachtrup, Nano Lett. **13**, 2738 (2013).

[19] N. Aslam, M. Pfender, P. Neumann, R. Reuter, A. Zappe, F. F. de Oliveira, A. Denisenko, H. Sumiya, S. Onoda, J. Isoya, and J. Wrachtrup, Science **357**, 67 (2017).

[20] D. R. Glenn, D. B. Bucher, J. Lee, M. D. Lukin, H. Park, and R. L. Walsworth, Nature (London) **555**, 351 (2018).

[21] L. J. Rogers, K. L. D. Jahnke, L. Marseglia, C. Müller, B. Naydenov, H. Schauffert, C. Kranz, T. Teraji, J. Isoya, L. P. McGuinness, and F. Jelezko, Nat. Commun. **5**, 4739 (2014).

[22] A. Sipahigil, K. D. Jahnke, L. J. Rogers, T. Teraji, J. Isoya, A. S. Zibrov, F. Jelezko, and M. D. Lukin, Phys. Rev. Lett. **113**, 113602 (2014).

[23] L. J. Rogers, K. D. Jahnke, M. H. Metsch, A. Sipahigil, J. M. Binder, T. Teraji, H. Sumiya, J. Isoya, M. D. Lukin, P. Hemmer, and F. Jelezko, Phys. Rev. Lett. **113**, 263602 (2014).

[24] D. D. Sukachev, A. Sipahigil, C. T. Nguyen, M. K. Bhaskar, R. E. Evans, F. Jelezko, and M. D. Lukin, Phys. Rev. Lett. **119**, 223602 (2017).

[25] J. N. Becker, B. Pingault, D. Groß, M. Gündoğan, N. Kukharchyk, M. Markham, A. Edmonds, M. Atatüre, P. Bushev, and C. Becher, Phys. Rev. Lett. **120**, 053603 (2018).

[26] T. Iwasaki, F. Ishibashi, Y. Miyamoto, Y. Doi, S. Kobatashi, T. Miyazaki, K. Tahara, K. D. Jahnke, L. T. Rogers, B. Naydenov, F. Jelezko, S. Yamasaki, S. Nagamachi, T. Inubushi, N. Mizuochi, and M. Hatano, Sci. Rep. **5**, 12882 (2015).

[27] P. Siyushev, M. H. Metsch, A. Ijaz, J. M. Binder, M. K. Bhaskar, D. D. Sukachev, A. Sipahigil, R. E. Evans, C. T. Nguyen, M. D. Lukin *et al.*, Phys. Rev. B **96**, 081201(R) (2017).

[28] Y. N. Palyanov, I. N. Kupriyanov, Y. M. Borzdov, and N. V. Surovtsev, Sci. Rep. **5**, 14789 (2015).

[29] T. Iwasaki, Y. Miyamoto, T. Taniguchi, P. Siyushev, M. H. Metsch, F. Jelezko, and M. Hatano, Phys. Rev. Lett. **119**, 253601 (2017).

[30] A. E. Rugar, C. Dory, S. Sun, and J. Vučković, Phys. Rev. B **99**, 205417 (2019).

[31] C. Bradac, W. Gao, J. Forneris, M. E. Trusheimb, and I. Aharonovich, Nature Commun. **10**, 5625 (2019).

[32] J. P. Goss, P. R. Briddon, M. J. Rayson, S. J. Sque, and R. Jones, Phys. Rev. B **72**, 035214 (2005).

[33] B. L. Cann, Ph.D. thesis, University of Warwick, Coventry, UK, 2009.

[34] C. B. Hartland, Ph.D. thesis, University of Warwick, Coventry, UK, 2014.

[35] G. Thiering and A. Gali, Phys. Rev. B **94**, 125202 (2016).

[36] Y. G. Zhang, Z. Tang, X. G. Zhao, G. D. Cheng, Y. Tu, W. T. Cong, W. Peng, Z. Q. Zhu, and J. H. Chu, Appl. Phys. Lett. **105**, 052107 (2014).

[37] A. Kunisaki, M. Muruganathan, H. Mizuta, and T. Kodera, Jpn. J. Appl. Phys. **56**, 04CK02 (2017).

[38] M. Muruganathan and H. Mizuta, Diamond Relat. Mater. **114**, 108341 (2021).

[39] S. Felton, A. M. Edmonds, M. E. Newton, P. M. Martineau, D. Fisher, D. J. Twitchen, and J. M. Baker, Phys. Rev. B **79**, 075203 (2009).

[40] H. Sumiya and H. Satoh, Diamond Relat. Mater. **5**, 1359 (1996).

[41] A. M. Portis, Phys. Rev. **100**, 1219 (1955).

[42] A. M. Edmonds, U. F. S. D'Haenens-Johansson, R. J. Cruddace, M. E. Newton, K.-M. C. Fu, C. Santori, R. G. Beausoleil, D. J. Twitchen, M. L. Markham *et al.*, Phys. Rev. B **86**, 035201 (2012).

[43] J. S. Hyde, Phys. Rev. **119**, 1483 (1960).

[44] V. A. Livshits and D. Marsh, J. Magn. Res. **175**, 317 (2005).

[45] J. H. N. Loubser and J. A. van Wyk, *Diamond Research 1977*, edited by P. Daniel (De Beers Industrial Diamond Division, Ascot, 1977), pp. 11–14.

[46] S. Felton, A. M. Edmonds, M. E. Newton, P. M. Martineau, D. Fisher, and D. J. Twitchen, Phys. Rev. B **77**, 081201(R) (2008).

[47] C. M. Hofmann, M. Ludwig, P. Christmann, D. Volm, B. K. Meyer, L. Pereira, L. Santos, and E. Pereira, Phys. Rev. B **50**, 17618 (1994).

[48] N. T. Son, X. T. Trinh, L. S. Løvlie, B. G. Svensson, K. Kawahara, J. Suda, T. Kimoto, T. Umeda, J. Isoya, T. Makino, T. Ohshima, and E. Janzén, Phys. Rev. Lett. **109**, 187603 (2012).

[49] *EPR Imaging and in Vivo EPR*, edited by G. R. Eaton, S. S. Eaton, and K. Ohno (CRC, Boca Raton, FL, 1991).

[50] M. Ikeya, Annu. Rev. Mater. Sci. **21**, 45 (1991).

[51] M. Furusawa and M. Ikeya, J. Phys. Soc. Jpn. **59**, 2340 (1990).

[52] G. A. Watt, M. E. Newton, and J. M. Baker, Diamond Relat. Mater. **10**, 1681 (2001).

[53] W. V. Smith, P. P. Sorokin, I. L. Gelles, and G. J. Lasher, Phys. Rev. **115**, 1546 (1959).

[54] A. Cox, M. E. Newton, and J. M. Baker, J. Phys. Condens. Matter **6**, 551 (1994).

[55] J. A. Weil, J. R. Bolton, and J. E. Wertz, *Electron Paramagnetic Resonance* (Wiley, New York, 1994).

[56] T. Umeda, S. Hagiwara, M. Katagiri, N. Mizuochi, and J. Isoya, Physica B **376–377**, 249 (2006).

[57] A. Gali, M. Fyta, and E. Kaxiras, Phys. Rev. B **77**, 155206 (2008).

[58] G. Thiering and A. Gali, Phys. Rev. B **96**, 081115(R) (2017).

[59] A. Gali, Nanophotonics **8**, 1907 (2019).

[60] J. R. Maze, A. Gali, E. Togan, Y. Chu, A. Trifonov, E. Kaxiras, and M. C. Lukin, New J. Phys. **13**, 025025 (2011).

[61] G. Thiering and A. Gali, Phys. Rev. B **98**, 085207 (2018).

[62] N. Aslam, G. Waldherr, P. Neumann, F. Jelezko, and J. Wrachtrup, New J. Phys. **15**, 013064 (2013).

[63] A. T. Collins and A. W. S. Williams, J. Phys. C **4**, 1789 (1971).

[64] R. C. Burns, V. Cvetkovic, C. N. Dodge, D. J. F. Evans, M.-L. T. Rooney, P. M. Spear, and C. M. Welbourn, J. Cryst. Growth **104**, 257 (1990).

[65] H. Kawarada, H. Matsuyama, Y. Yokota, T. Sogi, A. Yamaguchi, and A. Hiraki, Phys. Rev. B **47**, 3633 (1993).

[66] J. Barjon, T. Tillocher, N. Habka, O. Brinza, J. Achard, R. Issaoui, F. Silva, C. Mer, and P. Bergonzo, Phys. Rev. B **83**, 073201 (2011).

[67] R. M. Chrenko, H. M. Strong, and R. E. Tuft, Philos. Mag. **23**, 313 (1971).

[68] R. G. Farrer, Solid State Commun. **7**, 685 (1969).

[69] P. Deák, B. Aradi, M. Kaviani, T. Frauenheim, and A. Gali, Phys. Rev. B **89**, 075203 (2014).

[70] M.-L. T. Rooney, J. Cryst. Growth **116**, 15 (1992).

[71] D. Howell, A. T. Collins, L. C. Loudin, P. L. Diggle, U. F. S. D'Haenens-Johansson, K. V. Smit, A. N. Katrusha, J. E. Butler, and F. Nestola, Diamond Relat. Mater. **96**, 207 (2019).

[72] S. Satoh, H. Sumiya, K. Tsuji, and S. Yazu, *Science and Technology of New Diamond: Proceedings of the 1st Int. Conf. of New Diamond Science and Technology, Tokyo, Japan, October 24-26, 1988*, edited by S. Saito, O. Fukunaga, and M. Yoshikawa (KTK Scientific/Terra Scientific, Tokyo, 1990), pp. 351–355.

[73] A. T. Collins, J. Phys.: Condens. Matter **14**, 3743 (2002).

[74] A. T. Collins and G. S. Woods, J. Phys. C **20**, L797 (1987).

[75] S. Johnson, P. R. Dolan, and J. M. Smith, Prog. Quantum Electron. **55**, 129 (2017).

[76] A. M. Zaitsev, *Optical Properties of Diamondd: A Data Handbook* (Springer, Berlin, Heidelberg, New York, 2010), p. 298.

[77] A. M. Zaitsev, *Optical Properties of Diamond: A Data Handbook* (Springer, Berlin, Heidelberg, New York, 2010), p. 262.

[78] J. A. Freitas, Jr., P. B. Klein, and A. T. Collins, Electronics Lett. **29**, 1727 (1993).